# Non-iterative beamforming based on Huygens principle for multistatic UWB radar: application to breast imaging

Navid Ghavami[1], Penny Probert Smith[1], Gianluigi Tiberi[2], David Edwards[1] and Ian Craddock[3]

[1]Dept of Engineering Science, University of Oxford, Parks Road, Oxford, UK

[2]Fondazione Imago7, Viale del Tirreno, I-56128 Pisa, Italy

[3]Centre for Communications Research, Dept of Electrical and Electronic Engineering, University of Bristol.

**Abstract**

This paper examines the performance of a simple microwave beamforming method using the Huygens scattering principle (called here the HP method) for detecting breast lesions. The beamforming method is similar to non-iterative time reversal in that the wave received is propagated back into the material, although differs in its treatment of attenuation. The single pass algorithm does not require a solution to an inverse model, making it computationally efficient and so able to offer a throughput appropriate for clinical use. Its performance is compared with time delay beamforming, which may be implemented with similar computational complexity, on a set of phantoms, including a lossy medium, mimicking breast tissue. The method was used to image a commercially fabricated anatomically shaped breast phantom with multiple hidden inclusions mimicking tumours. The procedure was able to identify and localize significant scatterers inside the volume, with only approximate a-priori knowledge of the dielectric properties of the target object, in spite of its underlying assumption of a single scatterer model.

# 1 Introduction

Microwave imaging is an attractive and promising non-ionizing imaging modality for medical applications. An increasing number of research groups are investigating its applicability to breast cancer detection, motivated by the contrast in the dielectric properties of normal and malignant tissues at microwave frequencies [1–3]

Particular challenges in image reconstruction in this context are a low signal to noise ratio and poor resolution resulting from the long wavelength of microwaves and the complex scattering environment. There are two main classes of image reconstruction: microwave tomography [4–11] and UWB beamforming or radar techniques [1, 2, 12–14]. Microwave tomography techniques attempt to reconstruct dielectric properties by solving non linear inverse scattering problems, while UWB radar techniques solve simpler computational problems by seeking only to identify the significant scatterers inside the target volume. Although tomography offers the highest resolution, its high computational requirements mean that approximations are normally required to reach a throughput appropriate for a clinical environment, resulting in lower resolution (although a high resolution algorithm may be implemented efficiently using highly parallel computing) [4, 5, 15]. UWB beamforming techniques are computationally simpler and less dependent on prior model, although may still encounter difficulties in imaging spaces with a complex distribution of dielectric constant. They may be implemented in the time domain (when they are referred to as time delay beamforming) or frequency domain. Generic methods (normally implemented in the

frequency domain), based on optimizing signal to noise ratio, include the Capon filter and its robust formulation [16, 17] but deteriorate with errors in the forward model, and from correlation between receivers (a problem particularly in the context of high scattering and the wide angle of the receivers in microwave imaging), leading to rank deficiency in the noise matrix. Klemm has shown some advantage in using a physics based approach in [14], where signals are weighted at each grid point according to their conformity to a model of coherent detection.

Another class of image formation algorithms is time reversal [18]. Time reversal methods use Huygens' principle: given a set of measurements on the boundary, a consistent field can be reconstructed through treating the receivers as a set of sources. The signals received are back propagated towards the transmitter, and normally retransmitted in an iterative process until convergence. The back propagation normally uses an FDTD back propagation algorithm although a Green's function has also been suggested [19]. The method works on the principle that successive iterations reflecting at the measurement surfaces converge to a model of the strongest internal reflectors. Time reversal tolerates poor prior knowledge of the propagation coefficient in a lossless medium, but is strictly applicable only in lossless media. Modifications for attenuation in lossy media have been introduced [20, 21] but need prior knowledge of the attenuation characteristic.

For a lossless medium, the method described in this paper is similar to a single iteration of the time reversal method using the Green's function, which in turn, with an appropriate choice of Green's function, can be implemented as a time delay beamformer when the object is to reconstruct intensity rather

than electric field. Neither attempts to reconstruct the original field but simply to find regions of contrast. However the method differs from both in its treatment of attenuation. Comparison with the standard method of time delay beamforming over a set of simple phantoms suggest too an advantage in using incoherent rather than coherent addition over the set of transmitter positions. The subtraction of the mean field through summing the full set of signals received prior to time reversal, also allows reconstruction to take place using a very small number of transmitter positions, thus increasing the computational efficiency.

The method has previously been validated on canonical objects with single and multiple eccentric inclusions [20-22] through both 2-D and simple 3-D simulations and measurements. The experiments described in section 3 in this paper provide a more careful comparison with the standard implementation of the time delay algorithm, and investigate its use in lossy media. Section 4 describes its use in imaging a commercial 3-D breast phantom, designed to mimic the elastic properties of breast tumours for elastography imaging but with appropriate electrical properties as well.

Note that this paper addresses only 2-D image formation (with the 3-D image being made up of a set of independently imaged 2-D planes). Its extension to true 3-D imaging is discussed in the conclusions.

## 2 Methodology

This section presents the experimental configuration and the beamforming algorithms used.

## 2.1 Experimental configuration

Frequency-domain UWB measurements in an anechoic chamber were performed for all the measurements throughout this paper, using a vector network analyzer (VNA) arrangement to obtain the transfer function at 1601 discrete frequencies. Wideband UWB antennas, vertically polarised and omni-directional in the azimuth plane, were used. For each set of measurements, the location of a fixed transmitting antenna $m$ was fixed at approximately 20 cm away from the centre of the object, while the receiver antenna $n$ was positioned close to the external surface of the object and placed on a computer controlled rotating stage with 3° of angular resolution (Figure 1). Thus, the field $E_{nm}(f_l)$ was measured at $N = 120$ equally spaced points lying on the external circumference.

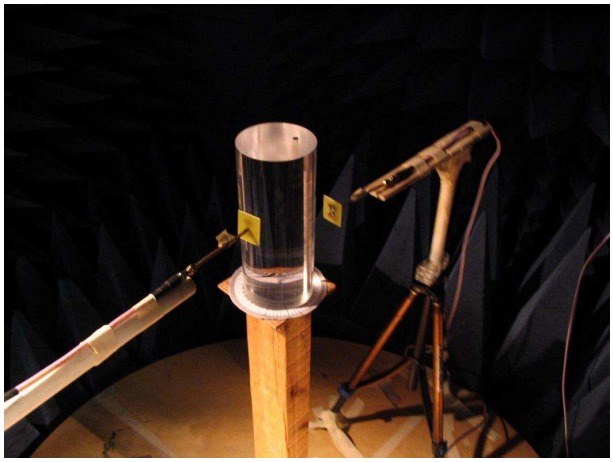

Figure 1: Measurement equipment, transmitting and receiving antennas are on the right and left sides of the figure, respectively.

## 2.2 Beamforming Algorithms

This section summarises the Huygens Principle (HP) method (more detail is given in [22]) and the time delay method. Because the results were obtained using a VNA, both algorithms were implemented in the frequency domain. A frequency domain implementation is also more efficient computationally than one in the time domain as it requires a matrix multiplication rather than shifts and summing of long arrays.

Consider a cylinder in free space. The cylinder is illuminated by a transmitting line source $\text{tx}_m$, $m = 1..M$ operating at a set of frequencies $f_l, l = 1..L$. Assume that there are $N$ receivers, with receiver $n$ at location $\boldsymbol{\rho}_n$ measuring field $E_{nm}(f_l)$ from receiver $m$ at frequency $f_l$. Assume that the dielectric properties in the bulk of the material is known. The problem is to identify the presence and location of discontinuities inside the cylinder from the fields measured at the receivers, $E_{nm}(f_l)$.

Consider now how to reconstruct a consistent field at location $\boldsymbol{\rho}$ within the cylinders. Allow the field received from transmitter $m$ at each receiver $n$ to re-radiate back isotropically within the cylinder. We calculate the field inside the cylinder as the superposition of these fields re-radiated by the $N$ receiving antenna to result in the reconstructed field $E_{\text{HP}}$. (where the subscript HP refers to the Huygens Principle method).

$$E_{\text{HP}}(\boldsymbol{\rho}, m, f_l) = \sum_{n=1}^{N} E_{nm}(f_l) G(k_l|\boldsymbol{\rho} - \boldsymbol{\rho}_n|) \tag{1}$$

where $G(k_l|\boldsymbol{\rho}_n - \boldsymbol{\rho}|)$ is the Green's function, defined as [22]:

$$G(k_l, \boldsymbol{\rho}, \boldsymbol{\rho}_n) = \frac{1}{4\pi} e^{-jk_l|\boldsymbol{\rho}-\boldsymbol{\rho}_n|} \tag{2}$$

and $k_l$ represents the wave number in the medium at frequency $f_l$. Note that $k_l$ is complex, to model both attenuation and phase delay.

Hence, substituting the Green's function into equation 1:

$$E_{\mathrm{HP}}(\boldsymbol{\rho}, m, f_l) = \frac{1}{4\pi} \sum_{n=1}^{N} E_{nm}(f_l) e^{-jk_l|\boldsymbol{\rho}-\boldsymbol{\rho}_n|} \tag{3}$$

During the initial simulations, it was observed that an image of the transmitter appeared in the result, which sometimes masked the area of interest. However, this transmitter image can be successfully removed by modifying (1) such that:

$$E'_{\mathrm{HP}}(\boldsymbol{\rho}, m, f_l) = \sum_{n=1}^{N} (E_{nm} - \mathrm{avg}_M\{E_{nm}\}) G(k_l, \boldsymbol{\rho}, \boldsymbol{\rho}_n) \tag{4}$$

where $\mathrm{avg}_M\{E_{nm}\}$ represents the average of signals obtained illuminating the object using $M$ different transmitter positions.

Over all transmitters the total intensity may be determined through coherent or incoherent addition. The Huygens method is formulated using incoherent addition so that the relationship between the different transmitter signals is not important. In this case the intensities are added:

$$I_{\mathrm{HP}}(\boldsymbol{\rho}) = \sum_{m=1}^{M} \left[ \sum_{l=1}^{L} E'_{\mathrm{HP}}(\boldsymbol{\rho}, m, f_l) \right]^2 \tag{5}$$

The time delay method is implemented similarly in the frequency domain as a phase delay method over the frequency sum of the phase corrected signals. However whereas the time reversal method delays the phase further, the standard time delay method advances their phase of the signals received back to the scatterer point of origin. An equivalent expression may be written down by substituting $E_{\mathrm{HP}}$ with $E_{\mathrm{TD}}$ where:

$$E_{\mathrm{TD}}(\boldsymbol{\rho}, m, f_l) = \frac{1}{4\pi} \sum_{n=1}^{N} E_{nm}(f_l) e^{+jk_l|\boldsymbol{\rho}-\boldsymbol{\rho}_n|} \tag{6}$$

However the time delay method is normally performed coherently across the transmitters so this implementation will be used. In coherent addition the fields received for each transmitter are added leading to the intensity of the resulting image $I$:

$$I_{\mathrm{TD}}(\boldsymbol{\rho}) = \left[ \sum_{m=1}^{M} \sum_{l=1}^{L} E'_{\mathrm{HP}}(\boldsymbol{\rho}, m, f_l) \right]^2 \tag{7}$$

By comparing equations 3 and 6 it is clear that the two solutions are identical apart from the sign of the exponential $e^{\pm jk_l}$. In a lossless medium this simply leads to a phase shift of $\pi$ in each term, and in the summation over all frequencies. Therefore the resulting intensities will be equal if the addition over all transmitters has the same coherence. However in a lossy medium the treatment of attenuation differs as well. Both the time delay and normal time reversal methods compensate for the attenuation by amplifying the signals to compensate for their attenuation, whereas the HP method does not attempt to mimic the real physical process but attenuates the signals

further on their return path. It therefore effectively attenuates the signal at greater depth. This seems to offer some advantages in clutter to noise ratio as shown in the experiments which follow. Similarly the use of incoherent rather than coherent addition results in better position accuracy (as shown in section 3.1), probably because it increases the robustness to phase errors from small errors in calibration.

# 3 Experiments and simulations

## 3.1 Numerical simulation: Multilayered object with an eccentric inclusion

Before proceeding to experiments, the Huygens and time delay methods were compared by simulating a 3-layer cylindrical object, which has realistic human body tissue properties assigned to its three layers. A thin external cylinder, representing human skin (radius 4.25 cm, thickness 0.2mm, $\varepsilon_{r1} = 41$ and $\sigma_2 = 0.8$ S/m [23]) was filled with a lowloss dielectric representing normal breast tissue (radius 4.05cm, $\varepsilon_{r1} = 10$ and $\sigma_1 = 0.8$ S/m). A cylindrical inclusion with axis parallel to the first and radius 3 mm, was assigned the electrical properties of malignant tissue ($\varepsilon_{r1} = 50$ and $\sigma_1 = 1$ S/m), and placed 1.5 cm away from the axis of the first cylinder, with centre on the positive y-axis.

The receiver-transmitter configuration was similar to that used in experiments (see section 2.1). The external cylinder was illuminated using 4 transmitter sources situated about 8 cm from the axis of the cylinder, with a frequency band of 1-3 GHz and spacing of 10 MHz. For each transmit-

ter and for each frequency, the field ($E_{nm}(f_l)$) at $N = 120$ evenly spaced points lying on the external circumference was calculated using the method presented in [24]. Finally, the internal field was reconstructed using the HP method to find $I_{\text{HPincoh}}$ (5). The skin properties were used to determine $k_l$, to match the field at the receivers. The time delay method was then applied to find the equivalent intensity field, $I_{\text{TDcoh}}$ (7).

Figures 2(a) and 2(b) show the normalized intensity obtained through Huygens and time delay, respectively. For clarity the image is adjusted by setting to zero all intensity values below 0.5. Those between 0.5 to 1 are expanded to fill the range from 0 to 1.

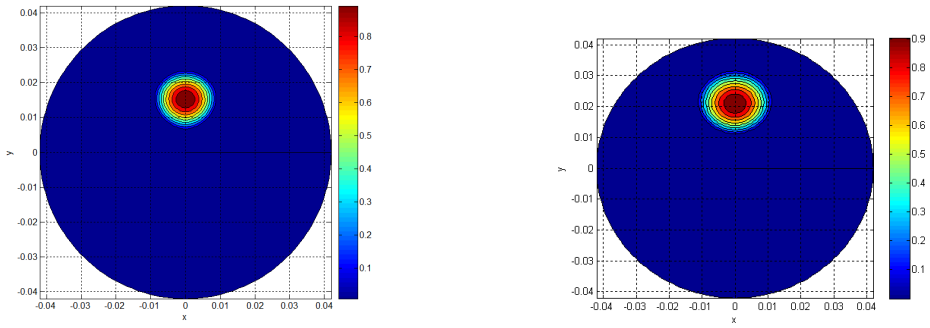

(a) (b)

Figure 2: Normalized intensity obtained through (a) HP procedure, (b) time delay. All scales are in meters.

The cylindrical inclusion is detected as a bright area in the image in both methods. The size is approximately the same. However, the time delay reconstruction places the inclusion at an offset of 0.75 cm in the y-axis, whereas the Huygens method detects the inclusion at its correct position (see Section 3.4).

The effect of reducing the number of transmitters and receivers was

also investigated. With only two transmitters, equivalent results in the HP method were obtained with as few as twelve receivers, whereas with four transmitters the number of receivers could be as few as four. The importance of multiple receivers was in the removing the mean; once this had taken place the image could be reconstructed using any of the transmitters. In general the deterioration in the HP method was slightly slower than in the TD method as receivers were removed but results were comparable.

### 3.2 Measurement 1: Cylinder with Multiple Inclusions

A low loss PMMA (polymethyl methacrylate) cylinder ($\varepsilon_{r1} = 2.7$, $\sigma_1 = 3 \times 10^{-7}$ S/m) with two inclusions was developed. One was a PEC (perfectly electrically conducting) cylinder, placed on the x-axis, with a radius of 3 mm. The other was placed by drilling a 3 mm radius hole from the PEC and filling it with an Agar-Agar solution concentration of approximately 6% (15g per 250g), leading to $\varepsilon_{r2} = 70$, $\sigma_2 = 1$ S/m. Each was placed at a distance of about 2.1 cm from the centre axis (See Figures 3(a) and 3(b)).

Bow-tie antennas and a frequency band of 6-8 GHz were used in the measurement. Six transmitter positions were used ($M = 6$), placed at angular increment of 60°. Figures 4(a) and 4(b) show the linear normalized intensity obtained through the two algorithms (equations 5 and 7). Two peaks with different intensities can be clearly detected using both methods. The peak with the higher intensity corresponds to the PEC cylinder (reflecting the greater contrast between P.M.M.A. and PEC), while the less intense peak represents the location of the Agar-Agar solution cylinder. An offset was observed in the location of the inclusions detected using the coherent

(a)

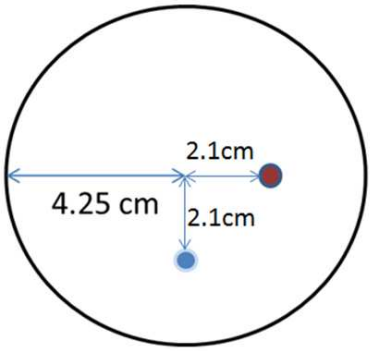


(b)

Figure 3: (a) Cast PMMA. cylinder having a radius of 4.25 cm with PEC and Agar-Agar solution inclusions. (b) Pictorial view of the problem, with the dark and light circles representing the PEC and Agar-Agar solution inclusions, respectively.

addition method (see Section 3.4). Since the loss is negligible, this experiment effectively compares coherent and incoherent addition and suggests that incoherent addition is the more robust.

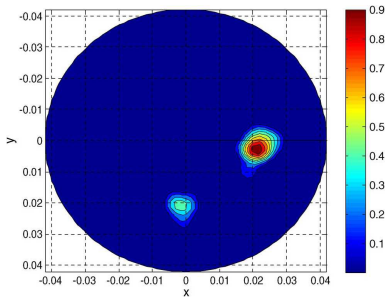


(a)

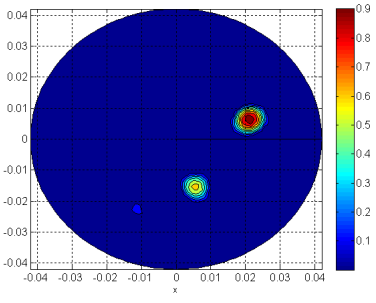


(b)

Figure 4: Normalized intensity obtained through (a) HP procedure, (b) time delay. All scales are in meters.

To investigate the effect of a near field, the transmitter was moved close

to the phantom (at a distance of about 1cm). The quality of the reconstruction was unchanged.

### 3.3 Measurement 2: Multilayered object with an eccentric inclusion

The next experiment introduced loss into the phantom as well as additional layers. A 2 mm thick PVC cylindrical pipe with radius of 5 cm was concentrically placed inside a larger plastic pipe, also 2 mm thick but with a larger radius of 6.25 cm. Both pipes were filled with agar-agar gel approximating a high water-content human tissue. A 3mm thick PEC rod representing a tumor was positioned eccentrically inside the gel [fig. 5(a)], at a distance of 3.25 cm from the axis of the cylinders [fig. 5(b)]. Although the thickness of the pipes was chosen to be as narrow as possible (2 mm), they had some effect on the effect on the image, making this model effectively a 5-layered problem.

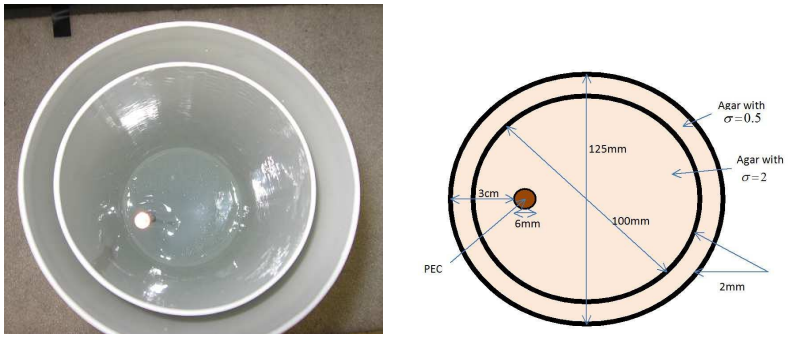


(a) (b)

Figure 5: (a) Multilayered medium with an inclusion, (b) Pictorial view of the problem

The agar-agar was dissolved in hot water at approximately 95°C and then cooled to room temperature to form a semi-transparent gel. The dielectric constant and the conductivity are functions of the concentration of the agar-agar [25]; for this experiment two distinct concentrations of Agar were used. Salt was added to vary the conductivity. The external plastic pipe was filled with a lower conductive agar-agar ($\sigma_1 = 0.5$ S/m), while the smaller plastic pipe was filled with a higher conductive agar-agar ($\sigma_1 = 2$ S/m). The change in the dielectric constant value was not notable and $\epsilon_r$ was assumed be 70 for both agar solutions. By comparing these values with those given in [26], it can be noted that the dielectric constant and the conductivity of agar-agar are similar to the actual dielectric properties of human tissues. In fact the loss-tangent of the agar-agar is even greater than that encountered in some human tissue imaging problems.

Discone antennas, vertically polarized and omni-directional in the azimuth plane were used. Measurements were recorded using a large frequency range of 1-10 GHz, using a frequency step of 5.6 MHz, with the extended frequency range being used because of the lossy medium. In addition, a 30 dB amplifier was used to increase the received signal.

As before the field $E_{nm}(f_l)$ at $N = 120$ equally azimuthally-spaced points lying on the external surface was measured. In this experiment four transmitter positions were used ($M = 4$) at angular increments of 90°. In this experiment the receiving antenna were not touching the gel and the free space value of $k$ produced better results in the HP reconstruction than the gel value (for which there was some distortion). Therefore an advantage of this configuration is that it removes the need to know the dielectric proper-

ties of the target volume.

Figures 6(a) and 6(b) show the linear normalised intensity obtained through HP and TD, respectively (see Section 3.4). Both methods successfully detect the inclusion, with a similar resolution, although a greater offset is present when employing the TD method.

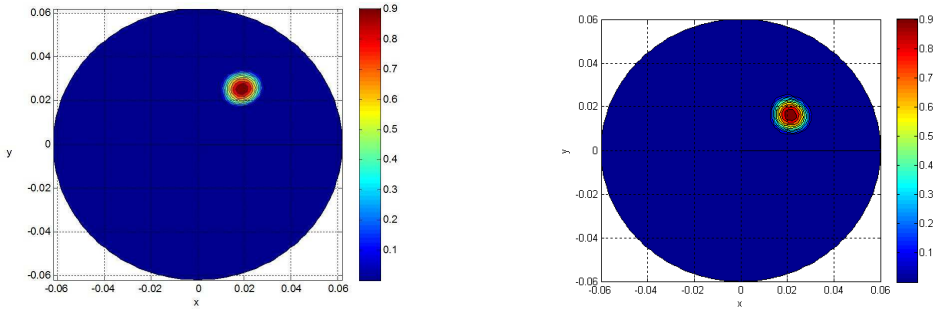


(a) (b)

Figure 6: Normalized intensity obtained through (a) HP procedure, (b) time-delay. All scales are in meters.

The effect of reducing the number of transmitters and receivers was also investigated in this more complex phantom. There was no noticeable deterioration in quality until the number of transmitter/receivers dropped below ten.

### 3.4 Assessment of imaging quality: Comparison of the methods

To compare the methods quantitatively three measures were used: the signal to clutter ratio (S/C), resolution and offset. The signal to clutter ratio (S/C) is defined as the ratio between the maximum inclusion response and the maximum clutter response in the same image [13]. Resolution is here

defined as the dimension of the region with normalized intensity greater than 0.5 (the 3 dB cutoff), and the offset is measured as the distance between the detected position of the inclusions and their actual location as observed during and after construction.

| | S/C (dB) | | Resolution (mm) | | Offset (cm) | |
|---|---|---|---|---|---|---|
| | HP | TD | HP | TD | HP | TD |
| 3-layer simulation | 3.5 | 3.2 | 6 | 6.2 | 0 | 0.6 |
| 5-layer measurement | 3.2 | 2.82 | 8 | 8 | 0.1 | 0.4 |
| Measurement with 2 inclusions | 2.7 | 2.75 | 4.5 | 4.5 | 0.2 | 0.5 |

Table 1: Comparison of the imaging methods

The results are shown in Table 1. The HP and TD methods perform similarly in terms of resolution, but the HP method gives more accurate positioning. For the more complex phantoms the HP has the better S/C ratio.

## 4 Experiment 3: A 3-D Breast Phantom

To assess the algorithm further it was tested on a commercial phantom sold for breast ultrasound elastography, the CIRS model-059 [27] ultrasonic breast phantom. As discussed below, fortuitously the electrical properties of this phantom, although, not completely known, are estimated to be in the right range for a reasonable assessment to be made. The use of this phantom allowed the system to be tested on a sample with an appropriate physical construction and a number of insertions of different size and a comparison to be made with elastography, a leading imaging method used to follow up mammography.

Although the phantom was three dimensional, it was imaged in 2-D slices. This type of imaging is often described as $2\frac{1}{2}$-D.

## 4.1 Properties of the Phantom

The phantom is approximately ellipsoidal in shape, 15 cm in length, 12 cm width and 7cm height at maximum, simulating the breast of an average patient in the supine position.

The phantom is made of a proprietary solid elastic water based polymer, known as Zerdine[28] (fig. 7), which is based on a polyacrylamide hydrogel [29]. It contains several randomly positioned solid masses (inclusions), 3-12 mm in diameter. It is designed to simulate the elasticity of breast tissue [30] with bulk material of stiffness around 20kPa, and inclusions of a few mm radius of at least twice that stiffness material, although with similar acoustic impedance.

Published work on polyacrylamide mixtures suggests that for material of stiffness 10kPa the refractive index of the bulk is around 1.5 [31]. Refractive index and density are related in polymer mixtures, with an approximately linear relationship suggested between dielectric constant (the square of refractive index) and density in this range [32]. Since the acoustic impedance of the insertions and the bulk are similar (the Zerdine masses are designed to be transparent to B-mode ultrasound) the density will be proportional to the elasticity. We would therefore expect approximately a doubling of dielectric constant between the bulk and the insertions, leading to a dielectric constant of around 9-10. Although these figures are very approximate, they suggest that the phantom is relevant as a test bed for microwave imaging,

although may offer less contrast than than a real tumour. Data on conductivity was unavailable but the response at high frequencies suggested that it may have been similar to that of the lossy phantom described in 3.3.

## 4.2 Elastography Imaging

Elastography imaging was used to locate the masses. Elastography is a non-invasive method in which stiffness or strain images of soft tissues are used to detect or classify tumours [33]. Because of higher stiffness, the tumour deforms less than the surrounding tissue when the sample is stressed either through palpitation on the surface or through applying a medium intensity ultrasound pulse locally) [34].

The Elastography imaging was performed using Sonix Systems' SonixTOUCH with the Elastography transducer. The transducer was applied with gently pressure to the phantom (through a thin layer of ultrasound gel) and moved slowly until an inclusion appeared on the Elastogram image (fig. 7). This procedure was repeated in all directions until the whole phantom surface is covered.

After a careful scan, 8 masses, varying in diameter between 8 and 12 mm were detected around the phantom (Table 2). The information from the Elastogram image was used to locate the position of the masses on a 3D hemisphere.

## 4.3 Microwave Imaging Results

The 3-D object was then imaged with the microwave system in a set of 2-D slices. Since elastography imaging results suggested that all the

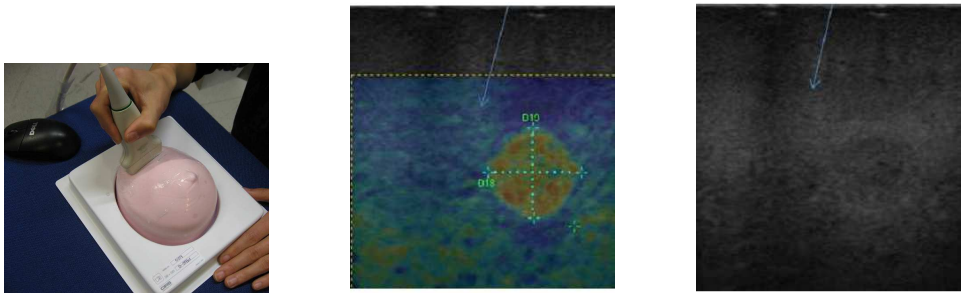

Figure 7: Left: Elastography scanning of the phantom; Centre: Typical elastography image of insertion. Right: B-mode image of same slice. Note that the inclusion is detected by Elastography whilst not by B-mode ultrasound, because of the close match in acoustic impedance.

| Inclusion | x-coordinate | y-coordinate | z-coordinate | diameter (mm) |
|---|---|---|---|---|
| 1 | 2.05 | -3.7 | 2.45 | 9 |
| 2 | -0.91 | 3.7 | 3 | 8.5 |
| 3 | 3.8 | 1.1 | 3.14 | 12 |
| 4 | 2.8 | 3.1 | 3.3 | 8 |
| 5 | 3.4 | 1.6 | 3.33 | 9.3 |
| 6 | 0.1 | -3.8 | 4.6 | 10 |
| 7 | -3.9 | 0.4 | 5 | 12 |
| 8 | -4 | 0 | 6 | 11.9 |

Table 2: Position (in cm) of the inclusions, estimated from elastography

inclusions were situated between 2 and 6 cm above the flat surface of the phantom (Table 2), four planar measurements were made in this region at 1 cm intervals using the discone antenna. Four pairs of cylindrical stands were placed to hold the antenna such that the centres of the antennas were placed at 2.5, 3.5, 4.5 and 5.5 cm above the surface of the phantom, respectively. Both transmitting and receiving discone antennas used were 1.5 cm long, enabling each measured cut to be fully covered by their signals.

The measurements were recorded using a frequency range of 1-10 GHz and a frequency sampling of 5.6 MHz, although observation of the $S_{21}$ magni-

tude, suggested that the useful frequency range was rather lower (a frequency range of 2-3 GHz was used in reconstruction). For each set of measurements, the location of the transmitting antenna was fixed at approximately 25 cm away from the centre of the breast phantom, while the receiver antenna was positioned roughly 1 cm away from the major axis surface of the phantom. For each slice, eight transmitter positions were used ($M = 8$), and the field was measured at $N = 120$ equally spaced points.

The HP method was applied to each slice. Figures 8(a)(a), (b), (c) and (d) show the linear normalized intensity obtained, corresponding to heights of 2.5, 3.5, 4.5 and 5.5 cm of the phantom above the flat surface, respectively.

In total, ten peaks of varying intensities can be clearly detected in the figures, six of which have been detected at approximately the same positions using the elastography machine, including, as expected, a cluster around a depth of 3.5cm. The four peaks which do not appear to correspond to the elastography estimates, may have been detected as mirror images [see figs. 8(a) and 8(b)], or may genuinely represent an inclusion undetected by the elastogram possibly due to their deep position inside the phantom (inner inclusion in fig. 8(c)).

Although the receiving antenna were not touching the phantom, better results were obtained through using values of propagation coefficient $k_l$ for the phantom (assuming $\epsilon_r = 10$), rather than air. The difference between this case and the previous one is the lower contrast ($\varepsilon_r = 10$ here whereas $\varepsilon_r = 70$ before) at the surface. Further work on identifying suitable values for $k_l$ is required.

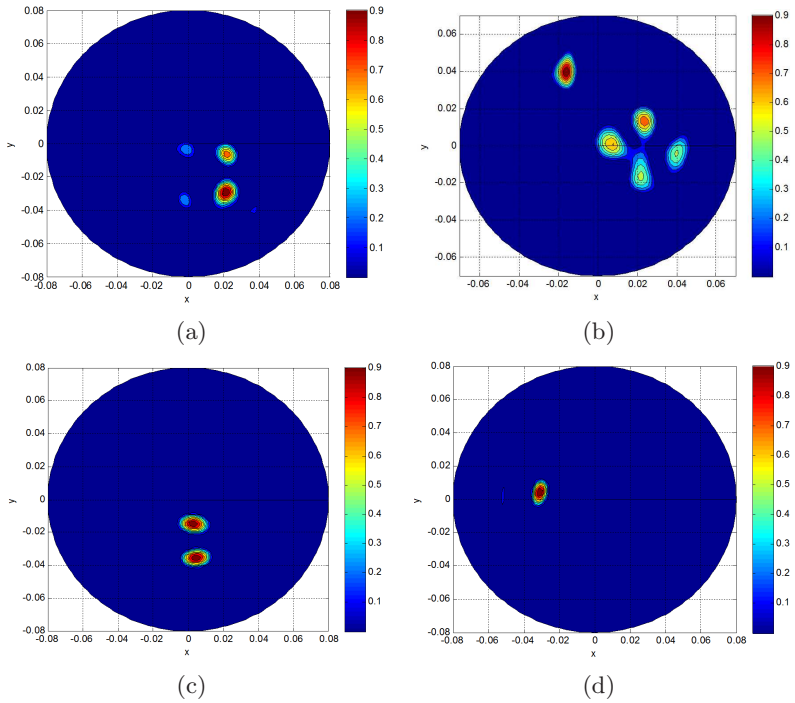


Figure 8: Linear normalised intensity, corresponding to heights (a) 2.5, (b) 3.5, (c) 4.5 and (d) 5.5 cm of the phantom above the flat surface, respectively.All axes in cm

## 5 Discussion and Conclusions

In this paper, the performance of a novel imaging method based on the Huygens principle (the HP method) was examined and compared with the time-delay method (TD), through a number of relatively simple simulations and measurements. Both methods are fast and cheap computationally [22]. Measurements and simulation in tissue-like phantoms suggest that the HP method results in improvements in positioning and signal to clutter ratio while giving a similar resolution. In addition the HP method appears to be more robust to sparse data, although both deteriorate once the spacing

of receivers falls below about 20°. Results on the elastography phantom suggest the method is a useful alternative to elastography, although more work is needed here to develop proper electrical phantoms.

Mathematically the HP and TD methods offer the same solution except in two respects. First, the HP method provides additional attenuation, especially at longer distances. This reduces noise, and was observed in the signal to clutter ratio. Although high frequency signals might be expected to be particularly affected, the resolution does not appear to degrade. However other types of filter, in distance or frequency, might improve the results further. Second, the HP method adds intensities rather than electric field over the sets of signals received from the different transmitters. Although such incoherent addition throws away information the results suggest that it offer advantages, probably because it is more robust to small errors in phase, resulting from poor calibration of antenna position or error in estimating the propagation coefficient. These are likely to be apparent particularly at high frequencies, because of the smaller wavelength. Robustness to errors in propagation coefficient is an advantage claimed by iterative methods, such as the iterative time reversal method (ITR). It would of course be possible in the HP or TD methods to iterate to an optimum (for example a search based on maximizing S/C ratio) but at computational cost. Further work is needed in determining how to choose the best propagation coefficient.

All three methods assume far field reconstruction. However both the HP and TD methods assume a single scatterer model, whereas the ITR implements a multi-scatterer model. However the ITR does not perform so well in lossy media since it is sensitive to the correct choice of attenuation.

The HP method is rather insensitive to this choice since it does not claim to reproduce the correct attenuation.

The challenge of developing robust methods to deal with materials with more complicated scattering regimes and geometries lie ahead. The results presented in this paper suggest that the HP method is worth further investigation as a candidate algorithm. Its computational simplicity makes it a suitable candidate for clinical applications.

## 6 Acknowledgements

This research was partially supported by UK Engineering and Physical Sciences Research Council and partially supported by a Marie Curie Intra European Fellowship within the 7th European Community Framework Program.

## References

[1] E. J. Bond, X. Li, S. C. Hagness, and B. D. Van Veen, "Microwave imaging via space-time beamforming for early detection of breast cancer," *IEEE Transactions on Antennas and Propagation*, vol. 51, no. 8, pp. 1690–1705, Aug. 2003.

[2] X. Li, S. K. Davis, S. C. Hagness, D. W. van der Weide, and B. D. Van Veen, "Microwave imaging via space-time beamforming: Experimental investigation of tumor detection inmultilayer breast phantoms," *IEEE Transactions on Microwave Theory and Techniques*, vol. 52, no. 8, pp. 1856–1865, Aug.2004.

[3] N. K. Nikolova, "Microwave imaging for breast cancer," *IEEE Microwave Magazine*, vol. 12, no. 7, pp. 78–94, Dec. 2011.

[4] P. M. Meaney and K. D. Paulsen, "Nonactive antenna compensation for fixed-array microwave imaging: Part II-Imaging results," *IEEE Trans. Med. Imag.*, vol. 18, no. 6, pp. 508–518, Jun. 1999.

[5] D. W. Winters, B. D. Van Veen and S. C. Hagness, "A Sparsity Regularization Approach to the Electromagnetic Inverse Scattering Problem", *IEEE Transactions on Antennas and Propagation*, Vol. 58, No. 1, Jan 2010, pp. 145-154.

[6] M. Donelli, I. Craddock, D. Gibbins, and M. Sarafianou, "A Three-Dimensional Time Domain Microwave Imaging Method for Breast Cancer Detection Based on an Evolutionary Algorithm", *Progress In Electromagnetics Research M*, Vol. 18, pp. 179-195, 2011.

[7] S. Kusiak and J. Sylvester, "The scattering support," Comm. Pure Appl. Math., vol. 56, no. 11, pp. 1525–1548, 2003.

[8] S. Kusiak and J. Sylvester, "The convex scattering support in a background medium," *SIAM J. Math. Anal.*, vol. 36, no. 4, pp. 1142-1148, 2005.

[9] M. Chiappe and G. L. Gragnani, "An analytical approach to the reconstruction of the radiating currents in inverse electromagnetic scattering", *Microwave and Optical Technology Letters*, vol. 49, n. 2, pp. 354-360, February 2007.

[10] G. L. Gragnani, "Two-dimensional non-radiating currents for imaging systems: theoretical development and preliminary assessment", *IET Microwaves, Antennas and Propagation*, vol. 3, n. 8, pp. 1164-1171, December 2009.

[11] X. Li and S. C. Hagness, "A confocal microwave imaging algorithm for breast cancer detection," *IEEE Microw. Wireless Compon. Lett.*, vol. 11, no. 3, pp. 130–132, Mar. 2001.

[12] A. Lazaro, D. Girbau and R. Villarino, "Simulated and Experimental Investigation of Microwave Imaging Using UWB", *Progress In Electromagnetics Research*, PIER 94, 263–280, 2009.

[13] E. C. Fear, X. Li, S. C. Hagness, and M. A. Stuchly, "Confocal microwave imaging for breast cancer detection: Localization of tumors in three dimensions," *IEEE Trans. Biomed. Eng.*, vol. 4, no. 8, pp. 812–822, Aug. 2002.

[14] M. Klemm, I. J. Craddock, J.A. Leendertz,A. Preece, and R. Benjamin, "Radar-based breast cancer detection using a hemispherical antenna array–Experimental results," *IEEE Transactions on Antennas and Propagation*, vol. 57, no. 6, pp. 1692–1704, Jun. 2009.

[15] J.-F. Deprez, M. Sarafianou, M. Klemm, I. J. Craddock, and P. J. Probert-Smith, "Microwave contrast imaging of breast tissue from local velocity estimation," Progress In Electromagnetics Research B, Vol. 42, 381-403, 2012.

[16] Petre Stoica, Randolph L. Moses, “Introduction to spectral analysis”, Prentice Hall, 1997.

[17] Yanwei Wang; Jian Li; Stoica, Petre, ”Rank-deficient robust Capon filter bank approach to complex spectral estimation,” Signal Processing, IEEE Transactions on , vol.53, no.8, pp.2713,2726, Aug. 2005.

[18] Fink, M., ”Time reversal of ultrasonic fields. I. Basic principles,” Ultrasonics, Ferroelectrics and Frequency Control, IEEE Transactions on , vol.39, no.5, pp.555,566, Sept. 1992.

[19] L. Jofre; A. Broquetas; J. Romeu; S. Blanch; A.P. Toda.; X. Fabregas; A. Cardama, “UWB Tomographic Radar Imaging of Penetrable and Impenetrable Objects,” Proceedings of the IEEE , vol.97, no.2, pp.451,464, Feb. 2009.

[20] Tanter, M.; Thomas, J.-L.; Fink, M., ”Focusing through skull with time reversal mirrors. Application to hyperthermia,” Ultrasonics Symposium, 1996. Proceedings., 1996 IEEE , vol.2, no., pp.1289,1293 vol.2, 3-6 Nov 1996.

[21] Mehmet Emre Yavuz, and Fernando L. Teixeira. “Ultrawideband Microwave Sensing and Imaging Using Time-Reversal Techniques: A Review”. Remote Sensing 2009, 9, 466-495

[22] N. Ghavami, G. Tiberi, D. J. Edwards, and A. Monorchio, “UWB Microwave Imaging of Objects With Canonical Shape,” *IEEE Transactions on Antennas and Propagation*, vol.60, no.1, pp.231-239, Jan. 2012.

[23] X. Li, S. K. Davis, S. C. Hagness, D. W. van der Weide, and B. D. Van Veen, "Microwave imaging via space-time beamforming: Experimental investigation of tumor detection in multilayer breast phantoms," *IEEE Trans. Microwave Theory Tech.*, vol. 52, no. 8, pp. 1856-1865, Aug. 2004.

[24] N. Ghavami, G. Tiberi, D. J. Edwards, A. Safaai-Jazi, and A. Monorchio, "Huygens principle based imaging of multilayered objects with inclusions," Progress In Electromagnetics Research B, Vol. 58, 139-149, 2014.

[25] K. Iizuka, "An agar-agar chamber for study of electromagnetic waves in an inhomogeneous medium", *IEEE Transactions on Antennas and Propagation*,Vol. 19 , Issue: 3, Year: 1971 , Page(s): 365 - 377

[26] C. Gabriel, S. Gabriely and E. Corthout, "The Dielectric Properties of Various Tissues" *Phys. Med. Biol.*, Vol. 41, p.p. 2231-2249, Year: 1996.

[27] Breast Elastography Phantom (model 059), "Computerized Imaging Reference Systems Inc",2008, 23513, Norfolk, Virginia, USA

[28] M. B. Zerhouni and M. Rachedine, Ultrasonic calibration material and method, U.S. Patent 5196343, Mar. 1993"

[29] Hungr N1, Long JA, Beix V, Troccaz, 'A realistic deformable prostate phantom for multimodal imaging and needle-insertion procedures: Supplementary Material I.' JMed Phys. 2012 Apr;39(4):2031-2041.

[30] J. Mende, M. Radicke, A. L. Kofahl, J. Schindler, D. Ulucay, J. Finsterbusch, B. Weber and K. Maier", "Detecting breast phantom lesions with acoustic radiation force in MR images: experiment and finite-element simulations", ISMRM 18th Scientific Meeting & Exhibition, Stockholm, May, 2010

[31] ML Byron, EA Variano "Refractive-index-matched hydrogel materials for measuring flow-structure interactions," Experiments in Fluids 54 (2), 1-6

[32] Lanza, V. L. and Herrmann, D. B. (1958), "The density dependence of the dielectric constant of polyethylene", J. Polym. Sci., 28: 622–625.

[33] Hatef Mehrabian and Abbas Samani, "An Iterative Hyperelastic Parameters Reconstruction for Breast Cancer Assessment",proc. of SPIE conference, vol. 6916, 2008.

[34] T. A. Krouskop, T. M. Wheeler, F. Kallel, B. S. Garra and T. Hall, "Elastic moduli of breast and prostate tissues under compression", *Ultrasonic Imaging*, vol. 20, pp. 260–274,